Integrating H2 synthesis and dynamic error budgetting for improved gravitational wave detection

Available online at www.sciencedirect.com

ScienceDirect

IFAC Papers Online CONFERENCE PAPER ARCHIVE

IFAC PapersOnLine 56-2 (2023) 3411–3416

Integrating $\mathcal{H}_2$ synthesis and Dynamic Error Budgetting for improved Gravitational Wave detection

Mathyn van Dael[1,3], Julia Casanueva[4], Gert Witvoet[1,2], Bas Swinkels[3], Manuel Pinto[4], Diego Bersanetti[5] Maddalena Mantovani[4], Camilla de Rossi[4], Piernicola Spinicelli[4], and Tom Oomen[1,6]

1 Eindhoven University of Technology, dept. of Mechanical Engineering, Control Systems Technology Eindhoven, The Netherlands, email: m.r.v.dael@tue.nl
2 TNO, Optomechatronics Department, Delft, The Netherlands
3 Nikhef, Amsterdam, The Netherlands
4 European Gravitational Observatory (EGO), I-56021 Cascina, Pisa, Italy
5 INFN, Sezione di Genova, I-16146 Genova, Italy
6 Delft Center for Systems and Control, Delft University of Technology, Delft, The Netherlands

Abstract: Dynamic error budgets are an essential tool in identifying opportunities for improvements in a control system for Gravitational Wave detectors, but their potential is often not fully utilized in the control design. This paper presents a model and dynamic error budget for a challenging nested control system in the Advanced Virgo detector in combination with a systematic control design framework for one of the controllers. This framework fully utilizes the dynamic error budget by using $\mathcal{H}_2$ synthesis to allow for fast iterations in the control design when dealing with conflicting control objectives. Simulations together with experimental results on Advanced Virgo illustrate the effectiveness of the presented framework.

Keywords: Modelling, error budget, systematic, $\mathcal{H}_2$, control design, Gravitational Waves

1. INTRODUCTION

Dynamic Error Budgets (DEBs) are an essential tool in identifying opportunities for control design improvements for Gravitational Wave (GW) detectors, see e.g. Cahillane et al. (2021), as the requirements on the sensitivity of the detectors such as Advanced Virgo (AdV) (Acernese et al., 2015) continuously increase. Even though the disturbances in GW detectors are mostly known, the development of these DEBs is not always straightforward as some control systems for example consist of nested loops, thus significantly increasing the complexity of the DEB. Precision requirements can furthermore be as stringent as 10×10^{-16} m Root Mean Square (RMS) and the degrees of freedom (DoF) of a GW detector are often strongly coupled (Allocca et al., 2020; van Dael et al., 2022). The model used for the DEB should therefore be sufficiently accurate and capture the different design considerations.

Although many such DEBs and control designs have been developed for different subsystems in GW detectors, at present no systematic framework exists in which the use of these DEBs are fully exploited in the control design. In e.g. Schütte (2016), $\mathcal{H}_2$ synthesis is proposed for the control of suspensions in GW detectors, but a full DEB is not considered in the optimization and the temporal behaviour of some of the disturbances (and hence practical aspects) is neglected. In Beker et al. (2014), a full DEB for one of the DoFs in a suspension system has been considered and an LQG control design has been presented, but the frequency dependent requirements on the performance variables are neglected in the synthesis. Combined with the fact that LQG and other algorithms alike are not straightforward to implement on this particular application makes decentralized control design the preferred choice of design method.

This paper presents a DEB for a challenging control system in AdV and uses this DEB to derive a systematic control design framework which fully exploits the DEB and maximizes the performance of the control system. The contribution of this paper is two-fold. The first contribution is the derivation and experimental verification of both the model and DEB and the second contribution is the development of a systematic control design framework that uses $\mathcal{H}_2$ synthesis to perform design trade-offs between the control objectives to yield a suitable control design. The second contribution will also illustrate how tools from the controls community can contribute to the simplification and analysis of a control design procedure for GW de-

⋆ This work has been funded by the Netherlands Organisation for Scientific Research (NWO) under grant number 680.92.18.02 and is also part of the research program VIDI with project number 15698, which is (partly) financed by the Netherlands Organisation for Scientific Research (NWO).

10.1016/j.ifacol.2023.10.1490

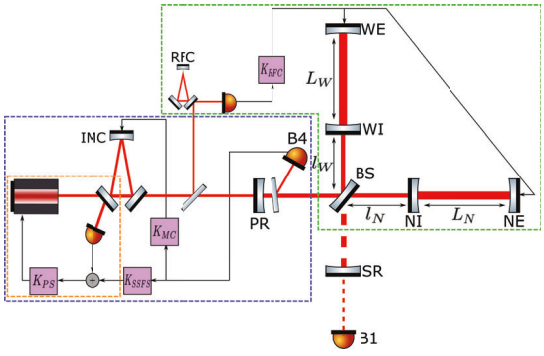

Fig. 1. The optical configuration of AdV, including the control scheme for the Common Arm. The B1 photodiode measures the interference pattern between the two arms ($l_W + L_W$ and $l_N + L_N$), which change in length with opposite signs when a GW passes. The two arms L_W and L_N are 3 km long.

tectors, as historically a lot of time has been spend on optimizing the control designs in the GW community.

The outline of this paper is as follows. In Section 2, a brief description of the AdV detector and the control system addressed in this paper is given together with an outline of the control challenge. The model and dynamic DEB for the control system considered in this paper are then presented in Section 3, after which a systematic design procedure is presented in Section 4. Experimental results measured on AdV are presented in Section 5 and a conclusion on the presented work is provided in Section 6.

2. PROBLEM FORMULATION

This section will present an overview of the system and formalizes the challenge addressed in this paper.

2.1 System description

Gravitational Wave detectors measure fluctuations in *spacetime* using optical interferometry. The interference pattern is determined by the difference in length between mirrors in two arms which are 3 km long. In Fig. 1, the optical layout of AdV is shown. The laser (left) creates a beam of light that is split by the Beam Splitter (BS) into two beams, going upwards and to the right. The beams travel 3 km (L_W and L_N) to the end mirrors (WE and NE) and are reflected back to interfere at the BS mirror. This interference pattern is measured by the B1 photodiode and is a function of the difference in length between the two arms L_W and L_N. In addition to the BS and end mirrors, there are an additional 4 mirrors (PR, SR, NI, WI) which contribute to enhancing the sensitivity of the detector. These mirrors form a total of 5 longitudinal DoFs (i.e. distances between mirrors) that are actively controlled by feedback systems. The most important DoF is the Differential ARM (DARM), given by

$$x_{\text{DARM}} = L_N - L_W, \tag{1}$$

which changes in length when a GW passes. The DARM DoF together with three of the other DoFs is controlled using a feedback system that actuates on the mirror positions and uses powers on the photodiodes to derive error signals, see van Dael et al. (2022) for a more detailed overview. The fifth DoF, the Common ARM (CARM) and given by

$$x_{\text{CARM}} = \frac{L_N + L_W}{2}, \tag{2}$$

is an outlier in terms of the actuation used to control this DoF. The two arms that form CARM are a set of Fabry-Perot cavities in which the light bounces up and down several hundred times to enhance the circulating power in the cavity. For the light to resonate in the cavity, the following condition has to be satisfied

$$x_{\text{cav}} = N \cdot \frac{\lambda}{2}, \tag{3}$$

where x_{cav} is the macroscopic length of the cavity in meters, λ the wavelength of the laser in meters and N an integer number. The cavities can thus be kept on resonance by either changing the length of the cavity to the corresponding laser wavelength, or by adjusting the wavelength of the laser to the cavity length. In the case of CARM, both actuation types are used in a set of nested loops because both the cavity length and laser frequency fluctuate too much when left uncontrolled.

2.2 Control system for CARM

This subsection will briefly highlight the different control loops for CARM, depicted in Fig. 1. The reader is referred to Acernese et al. (2009) for the reasoning behind the choice of control structure. The fastest loop is highlighted by the orange box and referred to as the Pre-Stabilization (PS) loop, in which the laser frequency is controlled with a bandwidth of 300 kHz to keep the Input Mode Cleaner (IMC) cavity on resonance. The Second Stage of Frequency Stabilization (SSFS) loop with a bandwidth of 7 kHz, highlighted by the blue box, provides a setpoint to the PS loop to bring the arm cavities on resonance. The RFC loop, highlighted by the green box, measures the laser frequency fluctuations and adjusts the length of CARM by actuating on the mirror positions with a bandwidth of 2 Hz to reduce the laser frequency fluctuations. With these three control loops closed, the arm cavities are kept on resonance while also minimizing the laser frequency fluctuations.

2.3 Problem formulation

The control system for CARM has been shown to be a complex system of nested loops. The control objective of this system is to ensure that the arm cavities are on resonance, but it is also essential to keep the laser frequency fluctuations to a minimum since they may lead to (non-linear) couplings (Calloni and Vajente, 2012; Acernese et al., 2009) to DARM. The challenge addressed in this paper is the derivation of a model and DEB and how to use this to improve the control system for CARM.

3. MODELLING AND DYNAMIC ERROR BUDGET

This section will present the model and DEB for the CARM loop. First, a key property for the model is derived after which the block diagram for the model is presented. The model is then experimentally verified and the DEB for CARM is presented, showing the limiting disturbances.

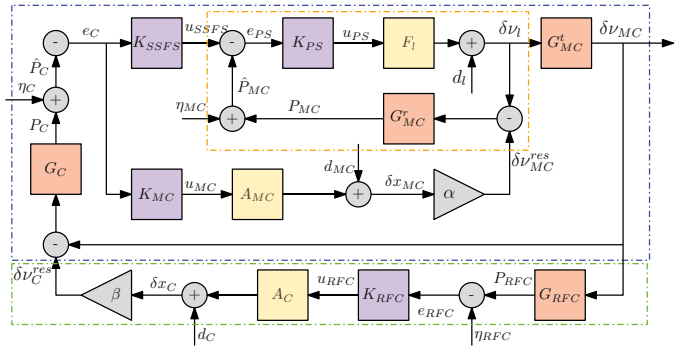

Fig. 2. Block diagram of the control scheme for CARM. The purple blocks denote controllers, the red blocks denote optical transfer functions and the yellow blocks denote mechanical transfer functions.

3.1 Model derivation

Recall that in order for a cavity to be on resonance, both the wavelength of the laser and cavity length must be controlled to satisfy (3). Controlling the wavelength is equivalent to controlling the laser frequency since

$$c = \lambda\nu, \tag{4}$$

where c is the speed of light and ν is the laser frequency. In order to model the control system in a block diagram, a relation between the laser frequency and cavity length is required. Based on (3), we can define

$$\frac{\delta\lambda}{\lambda_0} = \frac{\delta x}{x_0} \tag{5}$$

with $\lambda_0 = 1064\,\text{nm}$, x_0 the nominal length of the cavity and $\delta\lambda$, δx the fluctuations around the nominal wavelength and cavity length respectively. From (4) we find that

$$\frac{\delta\lambda}{\lambda_0} = -\frac{\delta\nu}{\nu_0}, \tag{6}$$

with $\delta\nu$ the laser frequency fluctuations and ν_0 the nominal laser frequency. Equations (4), (5) and (6) can then be combined to find a direct relation between $\delta\nu$ and δx, i.e.

$$\delta\nu = -\frac{c}{\lambda_0 x_0}\delta x. \tag{7}$$

It thus holds for small fluctuations of the laser frequency and cavity length that

$$\delta\nu + \frac{c}{\lambda_0 x_0}\delta x = \delta\nu - \gamma\delta x = \delta\nu - \delta\nu^{\text{res}} = 0 \tag{8}$$

with

$$\gamma(x_0) = -\frac{c}{\lambda_0 x_0}. \tag{9}$$

The second to last term in (8) intuitively shows how the resonance frequency of the cavity $\delta\nu^{\text{res}}$ is set by the cavity length and can be translated to a frequency using the constant γ. The cavity is then on resonance when the difference between the laser frequency and resonance frequency of the cavity is zero. Note that N can be any value as long as (3) is satisfied. The block diagram for the control system of CARM is depicted in Fig. 2. The nested control loops have been highlighted using the same colored rectangular boxes as in Fig. 1 and the resonance conditions from (8) for the IMC and arm cavities are represented by the summation point on the right and bottom left respectively. The constants α and β are given by

$$\alpha = \gamma(144), \;\; \beta = \gamma(3000), \tag{10}$$

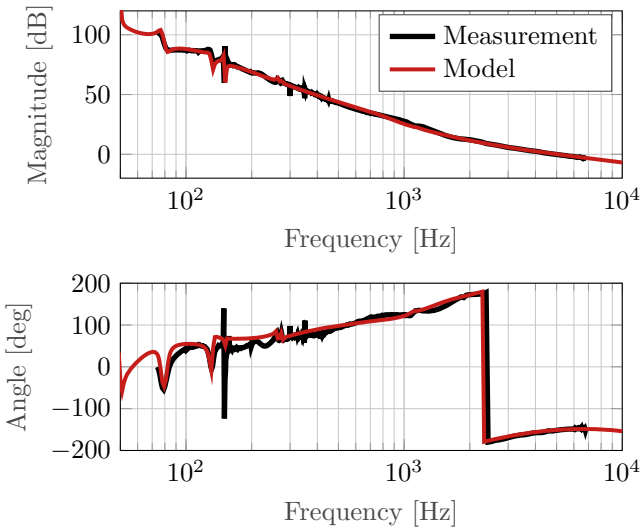

Fig. 3. Comparison of the modelled and identified frequency response for the SSFS loop to validate the low frequency (< 1 kHz) system dynamics.

since the nominal lengths of the IMC and arm cavities are 144 m and 3 km respectively. The output of the system is the laser frequency fluctuations $\delta\nu_{\text{MC}}$, which is the laser frequency going into the arms.

3.2 Model validation

Each block in Fig. 2 has been modelled as a transfer function using first principle modelling for the mechanics and optical simulations for the optics. The modelled versus measured frequency response of the SSFS loop will be presented next as this contains the most relevant and complicated dynamics of the system. The open-loop transfer function for this system is given by [1]

$$L_{\text{SSFS}} = G_{\text{C}} G^t_{\text{MC}} S_{\text{PS}} F_{\text{l}} K_{\text{PS}} \left(K_{\text{SSFS}} + G^r_{\text{MC}} \alpha A_{\text{MC}} K_{\text{MC}}\right) \tag{11}$$

with

$$S_{\text{PS}} = \left(1 + F_{\text{l}} K_{\text{PS}} G^r_{\text{MC}}\right)^{-1}. \tag{12}$$

The modelled and identified frequency response of L_{SSFS} are depicted in Fig. 3 and they are shown to be in good correspondence across almost the entire frequency range, bar some minor deviations around 150 Hz.

3.3 Dynamic Error budget

The final step in the modelling procedure is to model the disturbances and to compute their contributions to the output of the system using the closed-loop transfer functions for each disturbance. The following disturbances are considered in the model

$$w = \left[d_l \;\eta_{\text{MC}} \;d_{\text{MC}} \;\eta_{\text{C}} \;d_{\text{C}} \;\eta_{\text{RFC}}\right]^T, \tag{13}$$

with d_l the free running laser frequency fluctuations [2], η_{MC}, η_{C} and η_{RFC} the sensor noises for the IMC, CARM and RFC cavities respectively and d_{MC} and d_{C} the ground motion affecting the cavity lengths.

[1] The $(j\omega)$ is tacitly ommitted for each transfer function for brevity.
[2] "Free running" refers to the laser frequency fluctuations before they are attenuated by the control scheme as presented in Fig. 2

The contribution of each disturbance w to the performance variable $\delta\nu_{\mathrm{MC}}$ can then be computed using the frequency responses of the blocks according to

$$\begin{aligned}\mathcal{P}(\delta\nu_{MC}) &= \left|G^t_{\mathrm{MC}}S_{\mathrm{RFC}}S_{\mathrm{PS}}\right|^2\cdot\mathcal{P}(d_l)\\ &+\left|G^t_{\mathrm{MC}}S_{\mathrm{RFC}}S_{\mathrm{PS}}F_{\mathrm{l}}K_{\mathrm{PS}}\right|^2\cdot\mathcal{P}(\eta_{\mathrm{MC}})\\ &+\left|G^t_{\mathrm{MC}}S_{\mathrm{RFC}}S_{\mathrm{PS}}F_{\mathrm{l}}K_{\mathrm{PS}}G^r_{\mathrm{MC}}\alpha\right|^2\cdot\mathcal{P}(d_{\mathrm{MC}})\\ &+\left|G^t_{\mathrm{MC}}S_{\mathrm{RFC}}\mathcal{G}\right|^2\cdot\mathcal{P}(\eta_{\mathrm{C}})\\ &+\left|G^t_{\mathrm{MC}}S_{\mathrm{RFC}}\mathcal{G}G_C\beta\right|^2\cdot\mathcal{P}(d_{\mathrm{C}})\\ &+\left|G^t_{\mathrm{MC}}S_{\mathrm{RFC}}\mathcal{G}G_C\beta A_{\mathrm{C}}K_{\mathrm{RFC}}\right|^2\cdot\mathcal{P}(\eta_{\mathrm{RFC}})\end{aligned}\tag{14}$$

with

$$\begin{aligned}S_{\mathrm{RFC}} = (1+S_{\mathrm{PS}}F_{\mathrm{l}}K_{\mathrm{PS}}\left(K_{\mathrm{SSFS}}+G^r_{\mathrm{MC}}\alpha A_{\mathrm{MC}}K_{\mathrm{MC}}\right)\\ G_C(1+\beta A_{\mathrm{C}}K_{\mathrm{RFC}}G_{\mathrm{RFC}})G^t_{\mathrm{MC}})^{-1}\end{aligned}$$

and

$$\mathcal{G} = S_{\mathrm{PS}}F_{\mathrm{l}}K_{\mathrm{PS}}(K_{\mathrm{SSFS}}+G^r_{\mathrm{MC}}\alpha A_{\mathrm{MC}}K_{\mathrm{MC}}).\tag{15}$$

Here $\mathcal{P}(\cdot)$ denotes the Power Spectral Density (PSD) of a corresponding signal, which for each of the disturbances w_i equates to

$$\mathcal{P}(w_i) = |H_i|^2\cdot\mathcal{P}(\epsilon)\tag{16}$$

with $H_i(j\omega)$ a transfer function coloring the noise of the respective disturbance and ϵ is unit-power white noise.

The corresponding DEB is depicted in Fig. 4, showing the individual contributions of the disturbances and the measured $\delta\nu_{MC}$ in black, denoted by $\delta\hat{\nu}_{MC}$. The measurement $\delta\hat{\nu}_{MC}$ has been obtained by taking the in-loop error signal e_{RFC} and multiplying it by the inverse of G_{RFC} to obtain an estimate of the laser frequency fluctuations. Note that in this case the transfer function of η_{RFC} to the measured output is given by

$$\mathcal{P}(\delta\hat{\nu}_{MC}) = \left|G^{-1}_{\mathrm{RFC}}\right|^2\cdot\mathcal{P}(e_{\mathrm{RFC}}) = \left|G^{-1}_{\mathrm{RFC}}S_{\mathrm{RFC}}\right|^2\cdot\mathcal{P}(\eta_{\mathrm{RFC}})\tag{17}$$

which differs from the transfer function used in (14). In Fig. 4, $\eta^{\mathrm{in}}_{\mathrm{RFC}}$ therefore shows the contribution of η_{RFC} to the measured output using (17), whereas the last line in (14) is used to compute the expected true contribution of η_{RFC} to the laser frequency fluctuations $\delta\nu_{MC}$.

The modelled and measured laser frequency fluctuations are in good correspondence across the whole frequency range. Below 2 Hz, ground motion d_C is the dominant disturbance and this also dominates the RMS of $\delta\nu_{MC}$. Between 2 and 4 kHz, the measurement is dominated by the measurement noise η_{RFC} but this is an artefact of the chosen sensor, as η_{RFC} is only expected to be the dominant disturbance up to 10 Hz (dashed yellow line) above which the sensor noise η_C will limit the laser frequency fluctuations. The remainder of this work will focus on improving the control design to further suppress the RMS of the laser frequency fluctuations $\delta\nu_{MC}$.

4. $\mathcal{H}_2$ BASED CONTROL DESIGN

This section will present a control design framework that utilizes the DEB to setup $\mathcal{H}_2$ optimization for one of the controllers. First, a brief recap of $\mathcal{H}_2$ synthesis is given, after which the weighted plant used for synthesis is derived. A control design procedure using $\mathcal{H}_2$ synthesis is then presented and finally the coupling to DARM for each controller is assessed.

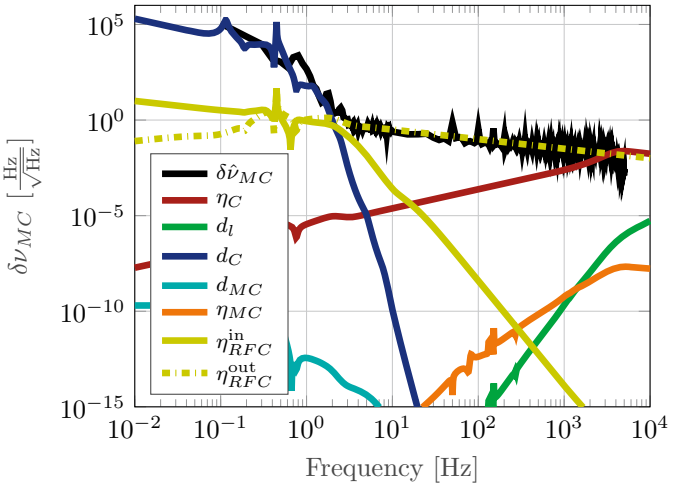

Fig. 4. DEB for the laser frequency fluctuations in AdV, illustrating the contributions of all disturbances to the output of the control system. The original controllers have been used to obtain the measurement.

4.1 $\mathcal{H}_2$ control theory

This section briefly recaps the theory behind $\mathcal{H}_2$ control. Any control problem can be formulated in the standard plant format

$$\begin{bmatrix}z\\y\end{bmatrix} = P\begin{bmatrix}w\\u\end{bmatrix}\tag{18}$$

where w are the exogenous inputs and z the outputs of the system and u, y the control variables. A $\mathcal{H}_2$ optimal controller then minimizes (Skogestad and Postlethwaite, 2005)

$$\|F(s)\|_2 = \sqrt{\frac{1}{2\pi}\int_{-\infty}^{\infty}\mathrm{tr}(F(j\omega)F(j\omega)^H)d\omega}\tag{19}$$

where $F(s)$ is the closed-loop function

$$F(s): w\rightarrow z,\tag{20}$$

which is equivalent to minimizing the RMS of z (Skogestad and Postlethwaite, 2005) when w is unit-power white noise.

4.2 Formulating the control problem

Section 3.3 showed that ground motion coupling to the arm mirrors is dominating the RMS of $\delta\nu_{\mathrm{MC}}$. The RFC loop is specifically implemented to reduce the laser frequency fluctuations and a new control design for K_{RFC} will therefore be derived in this section. The equivalent plant for K_{RFC} (i.e. the plant that K_{RFC} "sees") is given by

$$\begin{aligned}Q^{\mathrm{eq}}_{\mathrm{RFC}} = G_{\mathrm{C}}G_{\mathrm{RFC}}S_{\mathrm{SSFS}}G^t_{\mathrm{MC}}S_{\mathrm{PS}}F_{\mathrm{l}}K_{\mathrm{PS}}(K_{\mathrm{SSFS}}+\\ G^r_{\mathrm{MC}}\alpha A_{\mathrm{MC}}K_{\mathrm{MC}})\beta A_{\mathrm{C}}\end{aligned}\tag{21}$$

with

$$S_{\mathrm{SSFS}} = (1+L_{\mathrm{SSFS}})^{-1}.\tag{22}$$

Equation (21) can be simplified to

$$Q^{\mathrm{eq}}_{\mathrm{RFC}} = \beta G_{\mathrm{RFC}}A_{\mathrm{C}}T_{\mathrm{SSFS}} = \beta G_{\mathrm{RFC}}A_{\mathrm{C}}\tag{23}$$

since

$$T_{\mathrm{SSFS}}(j\omega) = 1-S_{\mathrm{SSFS}}(j\omega)\approx 1\,\forall\,\omega\ll 2\pi 7e3.\tag{24}$$

Since both β and G_{RFC} are simple gains in the frequency range of interest, the only block that contains any dynamics is A_{C}, making the plant fairly straightforward.

The next step is to define the exogenous inputs and outputs. The main control objective is to minimize $\delta\nu_{\mathrm{MC}}$, but for each control loop it holds that the coupling to DARM should be sufficiently small as to not spoil the detector sensitivity. The coupling from CARM to DARM stems from the inbalance between the two actuators acting on the end mirrors, producing a differential (DARM) motion when given a common (CARM) control signal. This coupling can be approximated by

$$x_{CtoD} = A_{\mathrm{C}} \cdot \rho \cdot u_{\mathrm{RFC}}, \tag{25}$$

where $\rho \in \mathbb{R}$ is the assumed actuator inbalance factor. Since the detection band of a GW detector starts at 10 Hz, the coupling from CARM to DARM must be sufficiently small above this frequency not to spoil the sensitivity. We therefore choose the following outputs

$$z = \left[\delta\nu_{\mathrm{MC}}\ u_{\mathrm{RFC}}\right]^T, \tag{26}$$

where a frequency dependent weighting on u_{RFC} is used to enforce sufficient roll-off in the control gain. The output weighting matrix is given by

$$V(s) = \mathrm{diag}([\kappa\ H_u(s)\ 1]) \tag{27}$$

with $\kappa \in \mathbb{R}$ a constant which can be used to change the relative importance of $\delta\nu_{\mathrm{MC}}$ with respect to u_{RFC} and H_u the inverse of an N order lowpass filter to enforce roll-off in the control gain.

For the exogenous inputs, only η_{C}, d_{C} and η_{RFC} are used in the synthesis as they are at some frequency range dominant in the DEB. The input weighting matrix for the controller synthesis is given by

$$W(s) = \mathrm{diag}([H_i(s)\ 1]), \tag{28}$$

where H_i are the disturbance models for the respective disturbances w_i. While the disturbance models for the sensor noises are simple gains, the disturbance model for d_{C} is more complicated. The mirrors of a GW detector are suspended by large-scale suspension systems (Braccini et al., 2005) to isolate the mirrors from ground motion. These suspensions consist of passive concatenated harmonic oscillators with very low eigenfrequencies (< 2 Hz), together with active feedback systems to damp the typically lowly damped modes of the harmonic oscillators. The mirror displacement can thus be represented by

$$d_{\mathrm{C}}(\omega) = X_{\mathrm{mir}}(\omega) = |X_{\mathrm{susp}}(j\omega)| \cdot X_{\mathrm{ground}}(\omega) = \left|\prod_i^M \frac{\psi_i^2}{(j\omega)^2 + 2\zeta_i\psi_i j\omega + \psi_i^2}\right| \cdot \frac{2\mathrm{e}{-6}}{\omega^2} \tag{29}$$

where $\psi_i \in \mathbb{R}^M$, $\zeta_i \in \mathbb{R}^M$ are the M suspension mode frequencies and damping factors respectively. The ground spectra is based on measurements of the ground motion at AdV (Fiori, 2015) and ψ, ζ have been estimated based on spectra of $\delta\nu_{\mathrm{MC}}$. There are however some uncertainties in this model which are important to consider in the control design. The first is that the ground motion varies over time, which is not captured in the model and thus the optimization. The second consideration is that a single suspension is modelled whereas CARM consists of four suspensions. There is thus some uncertainty in the locations of the suspension frequencies and damping.

The weighted plant is then given by

$$\tilde{P} = V \cdot P \cdot W, \tag{30}$$

which will be used for $\mathcal{H}_2$ controller synthesis.

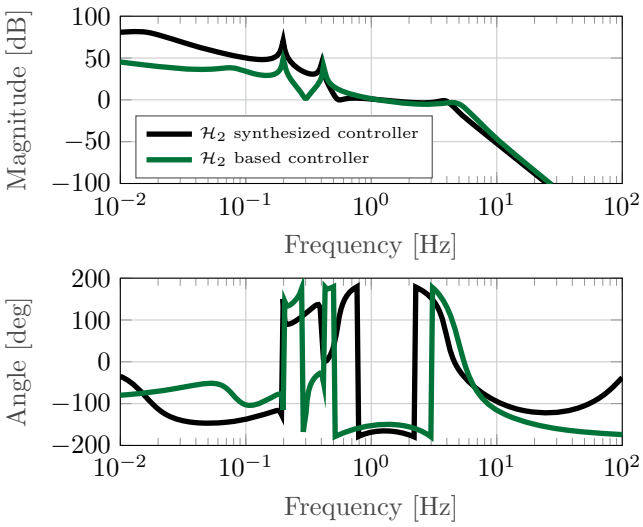

Fig. 5. Comparison between the open-loop transfer functions of the synthesized controller and the controller tuned based on this $\mathcal{H}_2$ optimal controller.

4.3 Controller design based on $\mathcal{H}_2$ synthesis

This section will present the $\mathcal{H}_2$ based control design which will be implemented at AdV. The $\mathcal{H}_2$ optimization is used to synthesize a controller on which a manual control design will be based. The reason why this controller is not directly implemented is two-fold. First, $\mathcal{H}_2$ synthesis does not provide guaranteed margins and the margins can thus be arbitrarily small, while a maximum of 6 dB sensitivity peak is desired for robustness. Second, as discussed in Section 4.2, there are some uncertainties in the suspension model. The $\mathcal{H}_2$ synthesis will produce a controller of the same order as the weighted plant, containing all the modelled suspension modes (which might differ slightly from the true suspension mode frequencies) and the synthesized controller is not always optimal due to the time-varying behaviour of the ground motion.

This knowledge is therefore used in the manual control design to obtain a low order version of the $\mathcal{H}_2$ optimal controller. A comparison between the open-loop transfer functions of the synthesized and manually tuned controllers is shown in Fig. 5, which shows a few key differences. First, to improve on the low margins of the synthesized controller, the poles for the roll-off are slightly shifted from 4 to 5 Hz and the anti-resonance at 0.5 Hz is shifted to 0.3 Hz, which will not decrease the performance too much since the ground motion in the model is overestimated with respect to a typical true ground spectrum. The consequence of the increased margins are a reduction in gain below the bandwidth, but the design choices have been made to maximize the gain in this region. The resonances at 0.2 and 0.4 Hz stem from the plant dynamics and are left undamped. This new controller will be implemented on AdV to compare its performance to the original controller.

4.4 Comparing the roll-off properties

While the minimization of $\delta\nu_{\mathrm{MC}}$ is the main objective of the RFC loop, the roll-off of the controller gain should also be sufficiently high not to spoil the DARM spectrum. The

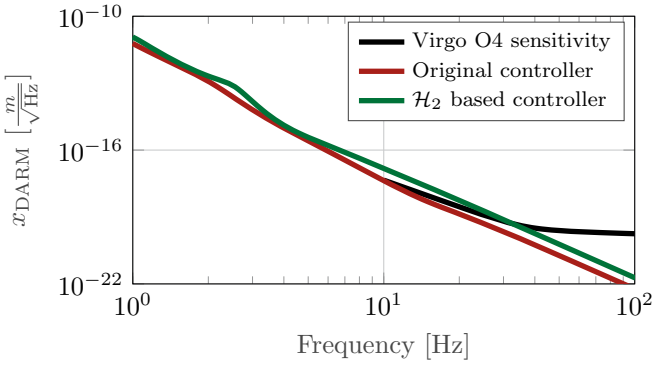

Fig. 6. Contribution of the CARM to DARM coupling for the original and new controller compared to the target DARM spectrum for the next science run of AdV.

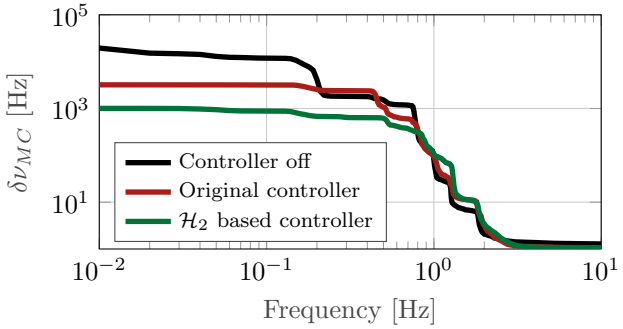

Fig. 7. Square root of Cumulative PSD for controller off, old and new $\mathcal{H}_2$ based controller. The lowest frequency bin is the total RMS of $\delta\nu_{MC}$

contribution of the coupling from CARM to DARM in (25) is therefore used to compare the roll-off properties of both controllers in Fig. 6 using $\rho = 0.01$, which is considered a worst-case scenario based on past experiences.

The old controller stays below the DARM target spectrum for all frequencies while the new controller is slightly above the target spectrum up to 15 Hz. The roll-off could be further increased by doing another design iteration, but is deemed sufficient for now since this is a worst case scenario.

5. EXPERIMENTAL RESULTS

The new controller has been implemented on AdV and the measurement results are depicted in Fig. 7. The new controller achieves roughly a factor 3 lower RMS compared to the original controller, at the expense of some loss in roll-off as shown in Section 4.4. The contributions to the total RMS in the 0.1 to 0.7 Hz region are furthermore minimal, indicating that not much more performance can be gained given the constraints on the roll-off.

6. CONCLUSION

An experimentally verified model and DEB have been presented in this paper for the CARM degree of freedom in AdV. The DEB is subsequently used to develop an $\mathcal{H}_2$ synthesis for one of the controllers and a manual control design is derived based on the synthesized controller. The framework allows for quick design iterations on the control design and deals with the stringent requirements on both the low frequency gain and high frequency roll-off properties. The derived controller is implemented on AdV and shows a factor 3 improvement in RMS at the expense of a small loss in roll-off around the start of the detection band of the detector.

ACKNOWLEDGEMENTS

The authors gratefully acknowledge the Italian Istituto Nazionale di Fisica Nucleare (INFN), the French Centre National de la Recherche Scientifique (CNRS) and the Netherlands Organization for Scientific Research, for the construction and operation of the Virgo detector and the creation and support of the EGO consortium. The authors also gratefully acknowledge research support from these agencies as well as by the Spanish Agencia Estatal de Investigación, the Consellera d'Innovació, Universitats, Ciència i Societat Digital de la Generalitat Valenciana and the CERCA Programme Generalitat de Catalunya, Spain, the National Science Centre of Poland and the Foundation for Polish Science (FNP), the European Commission, the Hungarian Scientific Research Fund (OTKA), the French Lyon Institute of Origins (LIO), the Belgian Fonds de la Recherche Scientifique (FRS-FNRS), Actions de Recherche Concertées (ARC) and Fonds Wetenschappelijk Onderzoek – Vlaanderen (FWO), Belgium.

REFERENCES

Acernese, F. et al. (2009). Laser with an in-loop relative frequency stability of 1.0×10^{-21} on a 100-ms time scale for gravitational-wave detection. *Phys. Rev. A*, 79, 053824.

Acernese, F. et al. (2015). Advanced Virgo: a second-generation interferometric gravitational wave detector. *Class. Quant. Grav.*, 32(2), 024001.

Allocca, A. et al. (2020). Interferometer Sensing and Control for the Advanced Virgo Experiment in the O3 Scientific Run. *Galaxies*, 8(4).

Beker, M.G. et al. (2014). State observers and Kalman filtering for high performance vibration isolation systems. *Rev Sci Instrum*, 85(3), 034501.

Braccini, S. et al. (2005). Measurement of the seismic attenuation performance of the VIRGO Superattenuator. *Astroparticle Physics*, 23(6), 557–565.

Cahillane, C., Mansell, G.L., and Sigg, D. (2021). Laser Frequency Noise in Next Generation Gravitational-Wave Detectors. *Optics Express*.

Calloni, E. and Vajente, G. (2012). Conceptual design of the second stage of frequency stabilization for Advanced Virgo. Technical Report VIR-0013C-12, EGO.

Fiori, I. (2015). Reference seismic data for Virgo. Technical Report VIR-0390A-15, The Virgo Collaboration.

Schütte, D. (2016). *Modern Control Approaches for Next-Generation Interferometric Gravitational Wave Detectors*. Ph.D. thesis, Gottfried Wilhelm Leibniz Universität Hannover.

Skogestad, S. and Postlethwaite, I. (2005). *Multivariable Feedback Control: Analysis and Design*. John Wiley & Sons, West Sussex, United Kingdom.

van Dael, M. et al. (2022). Design for interaction: Factorized Nyquist based control design applied to a Gravitational Wave detector. *in Proceedings of the 2022 Modelling, Estimation and Control Conference*.